

Beamforming-based Mitigation of Hovering Inaccuracy in UAV-Aided RFET

Suraj Suman, Swades De, Ranjan K. Mallik, Maged Elkashlan, and Arumugam Nallanathan

Abstract

Hovering inaccuracy of unmanned aerial vehicle (UAV) degrades the performance of UAV-aided radio frequency energy transfer (RFET). Such inaccuracy arises due to positioning error and rotational motion of UAV, which lead to localization mismatch (LM) and orientation mismatch (OM). In this paper, a hovering inaccuracy mitigation strategy in UAV antenna array beam steering based RFET is presented. The antenna beam does not accurately point towards the field sensor node due to rotational motion of the UAV along with pitch, roll, and yaw, which leads to deviation in the elevation angle. An analytical framework is developed to model this deviation, and its variation is estimated using the data collected through an experimental setup. Closed-form expressions of received power at the field node are obtained for the four cases arising from LM and OM. An optimization problem to estimate the optimal system parameters (transmit power, UAV hovering altitude, and antenna steering parameter) is formulated. The problem is proven to be nonconvex. Therefore, an algorithm is proposed to solve this problem. Simulation results demonstrate that the proposed framework significantly mitigates the hovering inaccuracy; compared to reported state-of-the-art the same performance can be achieved with substantially less transmit power.

Index Terms

Beam steering, Internet of Things, optimization, radio frequency energy transfer, UAV hovering inaccuracy, wireless sensors

I. INTRODUCTION

Unmanned aerial vehicles (UAVs) are used in recent times in various applications, such as defense and security, disaster management, surveillance and monitoring, healthcare, agriculture, telecommunication, and logistics [1]. The choice of UAVs lies in its several advantages, like excellent maneuverability, remote controllability, low cost, light weight, and programming flexibility. The usage of UAVs are also being envisaged for recharging the field deployed internet

S. Suman, S. De, and R. K. Mallik are with the Department of Electrical Engineering and Bharti School of Telecommunication, IIT Delhi, New Delhi, India. M. Elkashlan and A. Nallanathan are with the School of Electronic Engineering and Computer Science at Queen Mary University of London, UK.

of things devices (IoTDs), also called sensor nodes, through wireless power transfer (WPT) technology [2], where a UAV with a radio frequency (RF) transmitter mounted on it hovers above the IoTDs and charges them wirelessly. The mobility feature of the UAV enables it to access hard-to-reach inaccessible locations within a short time span to facilitate on-demand WPT. A UAV-aided WPT framework overcomes several challenges associated with real-life deployment, e.g., reachability to the field nodes due to infrastructure constraints, lack of cellular and electrical transmission infrastructure, and battery replacement with human intervention.

Automated and on-demand recharging of IoTDs is important to ensure their uninterrupted operation, since in many applications the IoTDs are tasked to sense the surroundings round the clock and report any undesired events to a central entity [3]. A major concern in 5G and beyond (B5G) is that the IoTDs consume significant amount of energy in sensing, processing, and communication [4]. A massively large number of IoTDs are envisioned to be used in various applications [5], such as smart farming, environmental sensing, area monitoring, security and defense, autonomous vehicles, smart city, smart home, and industrial automation, with almost 100% connectivity and availability [6]. [WPT has been found to be a promising solution to ensure the sustainable operation of 6G communication networks \[7\], \[8\].](#) Towards this goal, we believe that a UAV-aided WPT framework can potentially take the critical role of an automated recharging agent of the field nodes. Therefore, it is important to investigate the different limitations of UAV-aided WPT with a closer look on the feasibility in practical deployments. [Here, WPT refers to radiative WPT, which is also known as RF energy transfer \(RFET\) \[9\]. RFET works over a longer range, and data transfer as well as power transfer can be done over the same frequency band because RF waves carry energy as well as information. Off-the-shelf devices such as powercast energy harvesters \[10\] can be easily embedded with the sensor nodes to facilitate RFET.](#)

A. Related Work

The reported works related to UAV-aided RFET can be broadly classified in three categories: UAV-aided RFET only [11], [12], UAV-aided RFET and wireless information transfer (WIT) [13]–[19], and UAV-aided RFET, WIT, and mobile-edge computing (MEC) [20], [21]. The first set of works investigate strategies to recharge the field sensor nodes. Towards this, a UAV-mounted energy transmitter is deployed in [11] to deliver energy wirelessly to a set of nodes at known locations on the ground. The trajectory of the UAV is optimized to maximize the amount of energy transferred to the nodes during a finite charging period. In [12], the UAV supplies

wireless energy to a set of ground nodes aiming to maximize the minimum received energy among all the ground nodes. Here, a global optimal solution is achieved for the nodes deployed in a one-dimensional array as opposed to a local optimal solution in [11].

The second set of works studied to recharge the sensor nodes along with data collection from them through WIT. A wireless charging platform integrated with a quadcopter is reported in [13]. In [14], the UAV acts as an energy source to power device-to-device pairs for information transfer. Here, the resources are allocated in optimal sense to maximize the throughput within a time window. In [15], the UAV transfers energy to the user equipments in half-duplex or full-duplex mode, and the user equipments harvest energy for data transmission to the UAV. The total energy consumption of the UAV is minimized while satisfying the minimal data transmission requests of the user equipments. A UAV-assisted cooperative communication system based on simultaneous wireless information and power transfer (SWIPT) is presented in [16], wherein the UAV serves as a relay. Multiple UAVs are deployed as relays equipped with energy harvesting capability in [17]. In these works [16], [17], the UAV's transmission capability is powered by the energy harvested from RF signal transmitted from the source. The joint consideration of downlink SWIPT and uplink information transmission in UAV-assisted millimeter wave (mmWave) cellular networks is analyzed in [18]. On the other hand, the authors in [19] study the application of SWIPT to mmWave non-orthogonal multiple access (NOMA) enabled aerial networks, where an aerial base station sends wireless information and energy simultaneously via NOMA schemes to multiple single-antenna information decoding devices and energy harvesting devices.

The third set of works explored strategies to process the collected data locally on a UAV-mounted server followed by recharging and data collection from the sensor nodes. In [20], a UAV-enabled MEC wireless-powered system is studied. Here, the computation rate maximization problem is investigated, under both partial and binary computation offloading modes, subject to the energy-harvesting and the UAV's speed constraint. A time division multiple access based work flow model, which allows parallel transmissions and executions, is presented in [21] to improve energy efficiency of the UAV-enabled MEC wireless-powered system.

B. Motivation and Contribution

In the reported works [11]–[21], an ideal hovering condition of the UAV has been considered, which is not the case in real-life deployment. The operational condition of a UAV is very different from fixed static infrastructure, as it hovers above ground with sufficient payload. A

UAV experiences hovering inaccuracy due to various reasons, such as vibration and positioning errors. Recently, hovering inaccuracy of a UAV and its impact on the performance of UAV-aided RFET was measured and quantified in [22] through field experiments first time in the literature of UAV-aided RFET. Due to hovering inaccuracy, a UAV hovers at a position that is a little away from the desired position, leading to *localization mismatch (LM)*. It also undergoes rotational motion, leading to *orientation mismatch (OM)*. The individual as well as joint effects of these mismatches on UAV-aided RFET performance was analyzed. The study in [22] made the following observations on the effects of UAV hovering inaccuracy: (i) Compared to an ideal deployment scenario, a higher transmission power is required for the same RFET performance, (ii) optimum hovering altitude is significantly different, and (iii) compared to OM, the effect of LM is more severe.

The aforementioned observations reveal that the desired amount of energy is not harvested at IoTDS due to hovering inaccuracy of the UAV. The excess transmit power required to achieve the same set of objectives is a critical issue, because the UAV is an energy-limited system. Therefore, it is important to devise new strategies for mitigating the effects of hovering inaccuracy so that the energy loss due to this inaccuracy can be minimized in UAV-aided RFET. To the best of our knowledge, this is the first work in the literature of UAV-aided RFET where a mitigation strategy to overcome the performance degradation due hovering inaccuracy is studied.

The key considerations and contributions are as follows:

- 1) An array of antennas is mounted on the UAV to generate an optimally narrow beam directed towards the ground-deployed sensor node for recharging its battery. This antenna array offers a high gain with appropriate directivity to overcome the effect of LM.
- 2) OM leads to displaced beam spot on the ground, which does not ensure coverage of the sensor node. This happens due to deviation of elevation angle of the narrow antenna beam. To this end, an analytical framework to model the deviation in elevation angle is presented and its variation is estimated using the data collected through an experimental setup.
- 3) Closed-form expressions for the received power at the ground-deployed node are obtained for a total of four cases arising due to LM and OM. This enables us to investigate the mitigation capability of individual as well as joint degradation due to mismatch. A term *coverage probability* is defined, which plays a key role in evaluating the received power at the sensor node. Further, the received power is characterized for each of the four cases.
- 4) An optimization problem to estimate the optimal system parameters (transmit power, hover-

ing altitude of UAV, and antenna steering parameters) for mitigating the hovering inaccuracy is formulated. Simulation results reveal that the proposed framework mitigates the LM effectively, whereas the OM has appreciable adverse effect on the performance. However, the combined effect of LM and OM is mitigated significantly, and the same RFET performance is achieved with substantially less transmit power (up to 36% reduction) compared to [22].

5) A framework to analyze varying hovering inaccuracy is presented to evaluate the performance for different level of LM and OM. Numerical analysis reveals that, in contrast with the observation in [22], OM affects the performance more severely than LM.

This work distinguishes itself significantly from the previous work reported in [22]. The effects of UAV hovering inaccuracies on RFET were investigated in [22]. In contrast, the current study presents beamforming-based UAV hovering inaccuracy mitigation strategy to achieve a higher amount of energy transfer to a ground node. The consideration of beam steering approach entails a very different system model in presence of hovering inaccuracy and the associated performance analysis. Further, importantly, this study shows that, with beam steering the different aspects of hovering inaccuracy (LM and OM) have very different consequences and the associated optimization requirements.

C. Paper Organization

In Section II, the system model is presented. The effect of hovering inaccuracy on the system layout is analyzed in Section III. In Section IV, an optimization problem is formulated to estimate the optimal system parameters with hovering inaccuracy. The simulation results are discussed in Section V, followed by concluding remarks in Section VI.

II. SYSTEM MODEL

The system model for a UAV-aided RFET is shown in Fig. 1, where the antenna array is mounted at the bottom of the UAV. An antenna array radiates power over a narrow beam in a particular direction with high directivity. Excellent maneuvering capability of the UAV enables it to hover vertically above the sensor node and facilitate RFET. With this system configuration, hovering vertically above the sensor node offers the maximum received power, as the distance between transmitter and the individual receiver is minimum. There are several advantages of using a narrow beam compared to an omnidirectional radiation pattern. It transfers a higher amount of power to the ground sensor node due to higher directivity, which offers relatively

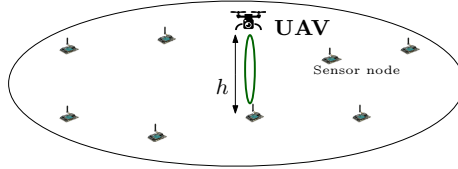


Figure 1: The system model for UAV-aided RFET.

higher coverage along the line-of-sight (LoS) to extend the range of RFET. This extended RFET range plays a key role in several real-life deployments. The UAV visits each field sensor node one by one and replenishes energy wirelessly, because the range of UAV-aided RFET is very small, up to a few meters only. This is due to relatively much higher minimum received power threshold (i.e., poor sensitivity) for RFET (approximately -12 dBm). On the other hand, inter-node distance in practical ground node deployment is much larger (e.g., ten meters or more) compared to the size (diameter) of the beam's ground projection (on the order of sub-meter). Thus, charging the nodes individually is only feasible with the narrow beam generated by UAV-mounted transmitter having limited ground projection area. Also, due to much smaller spot size compared to the inter-node distance, an individual node's charging process does not influence the charging process of another node. Simultaneous charging of multi-nodes through multi-beam is not beneficial because the gain and the power allocated to each beam are insufficient to meet the receive power threshold. Further, a large inter-node distance in real-life deployment degrades the energy harvesting capability due to higher path loss. Therefore, without loss of generality, for charging optimization, a single node is considered in the network. The consequence of the UAV hovering inaccuracy will be the same for charging any other ground node in the network. Since practically a UAV is able to charge one ground node at a time, the analysis of LM and OM can be extended to multi-UAV scenarios where each of them covers one node at a time without appreciable overlap of ground projection areas.

In the given context of UAV-aided RFET, the channel between the UAV and the sensor node is highly dominated by the LoS link due to smaller hovering altitude and limited ground projection area of the narrow beam. The effect of small-scale (multipath) fading is negligible with a narrow beam, i.e., when the LoS signal is very strong. Further, since the time required for RFET based charging is large (on the order of several minutes), and the effect of small-scale (multipath) fading is averaged out over such a long duration.

Referring to Fig. 1, the power received at a ground sensor node when the UAV hovers at

altitude h above it is expressed as

$$P(h, \theta) = P_{tx} G_{rx} F(\theta, \phi) \left(\frac{c}{4\pi f_c d_{tx-rx}} \right)^2 = \frac{P_{tx} \Lambda_0 F(\theta, \phi)}{[d_{tx-rx}]^2}, \text{ with } \Lambda_0 = G_{rx} \left(\frac{c}{4\pi f_c} \right)^2, \quad (1)$$

where P_{tx} is the radiated power transmitted by the transmitter mounted on the UAV and G_{rx} is the receiver antenna gain, c ($= 3 \times 10^8$ m/s) is the speed of light, f_c is the carrier frequency of the transmitted RF wave, d_{tx-rx} is the distance between transmitter and receiver, and $F(\theta, \phi)$ is the radiation pattern of the transmit antenna array, with θ and ϕ denoting, respectively, the elevation angle and the azimuth angle. $F(\theta, \phi)$ is expressed as [23]

$$F(\theta, \phi) = \begin{cases} N, & \text{if } \theta \in [-\theta_B(N)/2, \theta_B(N)/2], \phi \in [0, 2\pi] \\ 0, & \text{otherwise,} \end{cases} \quad (2)$$

where $\theta_B(N)$ is the half power beamwidth (HPBW) of the antenna array having N antenna elements and is $\theta_B(N) = \pi/\sqrt{N}$.

In the given context of UAV-aided RFET analysis, the main lobe of the antenna array is of our interest, because of its much higher gain compared to the side lobe gain. The impact of side lobe gain is negligible in RFET because the nodes are charged one-by-one individually due to smaller ground projection area of the narrow beam compared to the inter-node distance. Further, side lobe gain has no effect on the performance of UAV-aided RFET due to higher received power threshold (approximately -12 dBm) for RF energy replenishment. It is notable that, in contrast, the side lobe gain is of concern in cellular communication scenario due to much higher sensitivity for wireless information reception (i.e., it works even at much lower received power, -90 dBm or less), which causes interference [23].

Remark 1. *The ground node is equipped with an omnidirectional antenna, which aids in mitigation of LM of the hovering UAV. Moreover, omnidirectional circularly polarized antenna is a good choice, because of its insensitivity to polarization of the received signal [24].*

Remark 2. *The emphasis of the study is to analyze the impact of hovering inaccuracy on RFET performance, where the received power is considered as the performance metric due to analytical tractability. Since the harvested power is a non-decreasing function of the received power [25], the analysis for received power will also remain valid for harvested power [11], [12].*

III. EFFECT OF HOVERING INACCURACY ON SYSTEM LAYOUT

A. Analysis of Hovering Inaccuracy

The location of the ground sensor node to be charged is fetched into the UAV to schedule an autonomous flight, and it arrives at the mentioned location to facilitate RFET. It is desired that the UAV should hover vertically above the sensor node and remain stationary while facilitating RFET in order to transfer maximum energy to the ground sensor node, because this orientation offers the minimum distance between transmitter and receiver. Furthermore, the center of the transmitted beam should point towards the field sensor node. However, this does not happen in practical deployment due to hovering inaccuracy of the UAV [22]. In fact, the UAV hovers at a slightly different location rather than hovering vertically above the sensor node and undergoes rotation at this position. The UAV hovers at a different position other than the desired location due to positioning error caused by the global positioning system (GPS), which is termed as LM. The error caused due to rotation of the UAV is termed as OM.

In this work we explore the possibility that, in presence of hovering inaccuracy, the narrow beam generated by the UAV-mounted antenna array is steered towards the sensor node as shown in Fig. 2(a) using the location information of field deployed sensor node and the GPS mounted on the UAV. The location information of deployed sensor node is assumed known to the UAV, which can be either acquired during deployment of the sensor node or shared with the central entity (e.g., base station or UAV) during the field data transfer. This will overcome the effect of LM by providing a high gain. But OM displaces the center of the UAV-mounted antenna's beam pointed towards the sensor node as shown in Fig. 2(b). Thus, the repercussions of LM and OM lead to change in the system layout as depicted in Fig. 2(c). It is very important to investigate the effect of hovering inaccuracy on the system layout to analyze further the performance analysis of the UAV-aided RFET.

Remark 3. *First of all, the GPS coordinate system (represented using longitude and latitude) needs to be converted into Cartesian coordinate system. Let L_o^O and L_a^O be respectively the longitude and latitude of a location positioned on the ground at O . Then, the transformation from longitude and latitude to Cartesian coordinate is obtained as [26]*

$$x_O = R_e \cdot \cos(L_a^O) \cdot \cos(L_o^O), \quad y_O = R_e \cdot \cos(L_a^O) \cdot \sin(L_o^O)$$

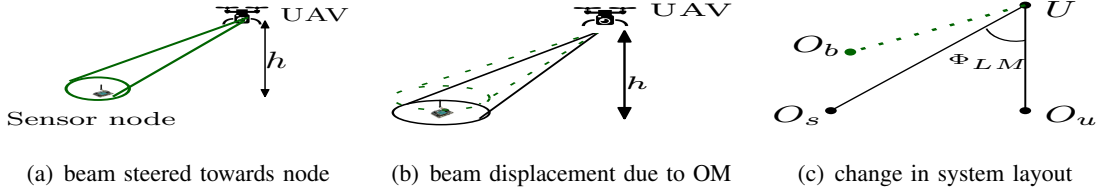


Figure 2: (a) UAV-mounted antenna's beam directed towards sensor node, (b) displacement of beam due to OM , and (c) geometrical interpretation of system layout due to hovering inaccuracy.

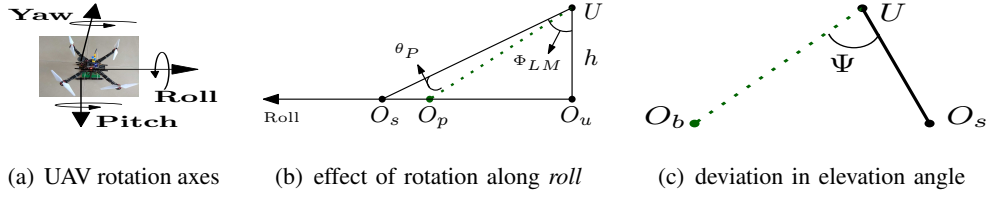


Figure 3: (a) The rotational axes of UAV; depiction of (b) rotation along *roll* and (c) deviation in elevation angle.

LM leads to change in distance and elevation angle between transmitter and receiver (Fig. 2(a)). Let $d(h)$ and $\Phi_{LM}(h)$ respectively denote the distance and elevation angle due to LM when the UAV hovers at altitude h . Let $O_s (x_s, y_s, 0)$ be the ground sensor node coordinate which can be obtained from Remark 4. The UAV hovers at location $U (x_u, y_u, h)$ which is not vertically above the location of the sensor node (Fig. 2(c)). Then, the location of the projection point of the UAV on ground above which it hovers is $O_u (x_u, y_u, 0)$. The distance $d(h)$ between transmitter and receiver is obtained as

$$d(h) = \|UO_s\| = \sqrt{(x_u - x_s)^2 + (y_u - y_s)^2 + h^2}. \quad (3)$$

The elevation angle $\Phi_{LM}(h)$ between UAV transmitter and ground receiver is

$$\Phi_{LM}(h) = \angle O_uUO_s = \arctan \left[\frac{\sqrt{(x_u - x_s)^2 + (y_u - y_s)^2}}{h} \right]. \quad (4)$$

The UAV undergoes rotational motion along its rotational axes. However, OM does not change the distance between transmitter and receiver. However, it displaces the narrow beam transmitted from the UAV-mounted antenna array towards the ground sensor node as shown in Fig. 2 (b). Thus, due to OM, the center of the antenna's beam does not accurately point towards the sensor node, which leads to deviation in the elevation angle $\angle O_sUO_b$ as shown in Fig. 2(c).

There are three types of rotational motion: *pitch*, *roll*, and *yaw*. *Pitch* corresponds to rotation around the lateral axis or around the wings, *roll* corresponds to rotation around the longitudinal axis or around the head, whereas *yaw* corresponds to rotation around the vertical plane. For convenience and analytical tractability, let us assume that *roll*, *pitch*, and *yaw* denote x , y , and z

axes, respectively, as shown in Fig. 3(a). With this assumption, Fig. 3(b) depicts the displacement of the beam center of the antenna array along *roll* axis, where the center of the beam points towards a slightly different location (say O_p) rather than the original sensor node's location O_s due to *roll* angle θ_R . Thus, the x -coordinate of the center of the displaced beam x_R due to rotation along the *roll* θ_R is obtained as

$$x_R = h \tan (\Phi_{LM} - \theta_R). \quad (5)$$

Likewise, y -coordinate of the displaced beam center y_P due to rotation along the *pitch* θ_P is

$$y_P = h \tan (\Phi_{LM} - \theta_P). \quad (6)$$

Thus, $(x_R, y_P, 0)$ is the new coordinate of the beam center after rotation along the *pitch* and *roll* axes. The beam experiences rotation along the *yaw*, which rotates the beam along the vertical z -axis and the beam experiences θ_Y angular rotation along the *yaw*. Consideration of the *yaw* is important, because radiation pattern of the transmitted beam from the UAV-mounted antenna array is not symmetric about the vertical axis (or z -axis). Thus, the antenna beam centered at $(x_R, y_P, 0)$ undergoes θ_Y angular rotation along the *yaw*. Then, the coordinate of the new center of the beam (say $O_b = (x_b, y_b, 0)$) after θ_Y rotation along the *yaw* (see Fig. 3 (c)) is obtained as

$$\begin{bmatrix} x_b \\ y_b \end{bmatrix} = \begin{bmatrix} \cos \theta_Y & -\sin \theta_Y \\ \sin \theta_Y & \cos \theta_Y \end{bmatrix} \begin{bmatrix} x_R \\ y_P \end{bmatrix} \Rightarrow \begin{aligned} x_b &= x_R \cos(\theta_Y) - y_P \sin(\theta_Y) \\ y_b &= x_R \sin(\theta_Y) + y_P \cos(\theta_Y). \end{aligned} \quad (7)$$

Finally, the center of the antenna's beam points towards $O_b (x_b, y_b, 0)$ (see Fig. 3 (c)) after experiencing the rotation of the UAV rather than the original sensor location O_s . This leads to the deviation in the elevation angle Ψ between the sensor node O_s and the shifted center of the beam spot O_b as shown in Fig. 3(c). Using the coordinates of the three points, i.e., the sensor node's location ($O_s \equiv (x_s, y_s, 0)$), the shifted center of the beam spot ($O_b \equiv (x_b, y_b, 0)$), and the UAV's location ($U \equiv (x_u, y_u, 0)$), the deviation in elevation angle Ψ is obtained as

$$\Psi = \angle O_b U O_s = \arccos \left[\frac{\overrightarrow{UO_b} \cdot \overrightarrow{UO_s}}{|\overrightarrow{UO_b}| \cdot |\overrightarrow{UO_s}|} \right]. \quad (8)$$

In (8), $\overrightarrow{UO_b} = [x_b - x_u, y_b - y_u, -h]$ and $\overrightarrow{UO_s} = [x_s - x_u, y_s - y_u, -h]$, and $\overrightarrow{UO_b} \cdot \overrightarrow{UO_s}$ denotes the dot product of two vectors $\overrightarrow{UO_b}$ and $\overrightarrow{UO_s}$.

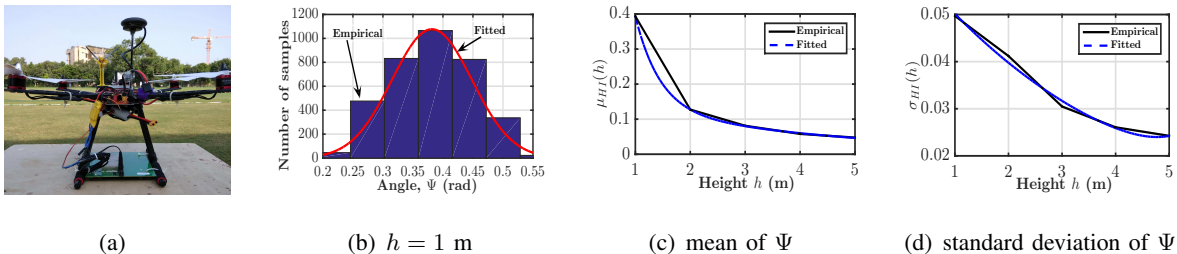


Figure 4: UAV experimental setup and variation of hovering inaccuracy parameters.

B. Modeling of Hovering Inaccuracy Parameter

For conducting experiments, a customized rotary-wing UAV was assembled (see Fig. 4(a)) and a single sensor node equipped with GPS module was considered. Extensive experiments were conducted in an open play ground. The GPS location of the deployed ground sensor node was noted. This position information along with the hovering altitude was fetched into the Ardupilot mission planner (<http://ardupilot.org>), which was installed in the computer acting as a ground control station. In the experiment, the setup was programmed to arrive at the fetched location and hover at altitudes ranging from 1 m to 5 m, for approximately three minutes at each altitude. While the UAV hovers at each of these altitudes statically, the rotation angle parameters, i.e., pitch, roll, and yaw, change frequently (around hundred samples per second). The data of the GPS location and the rotational motion parameters of the UAV were collected for further analysis. The hovering altitude of UAV was considered up to 5 meters only due to relatively higher received power threshold (i.e., poorer sensitivity) for RFET (approximately -12 dBm).

Using the GPS location data of the UAV and the sensor node at each hovering altitude h , the distance $d(h)$ and elevation angle $\Phi_{LM}(h)$ between the UAV-mounted transmitter and receiver on the ground are calculated for different hovering altitudes using (4) and (5), respectively. For this purpose, first the GPS coordinate system is converted into Cartesian coordinate system (see Remark 3). The estimated values of distance and elevation angle for different hovering altitude are modeled using curve fitting technique in order to obtain the empirical equations as function of hovering altitude for the ease of analysis. The empirical equations are given as

$$d(h) = \sqrt{u_1 h^2 + u_2 h + u_3} \quad \text{and} \quad \Phi_{LM}(h) = v_1 h^3 + v_2 h^2 + v_3 h + v_4 \quad (9)$$

where $u_1 = 1.015$, $u_2 = -0.1193$, $u_3 = 0.2588$, $v_1 = -0.01573$, $v_2 = 0.1763$, $v_3 = -0.651$, $v_4 = 0.8488$. The R-square values for the fitting of $d(h)$ and $\Phi_{LM}(h)$ are 0.9999 and 0.9938, respectively, and the values close to 1 indicate the best fit.

Table I: Variation of hovering inaccuracy parameters for beam steering based strategy

OM-only	$\Psi_{OM}(h) \sim \mathcal{N}(\mu_{OM}(h), \sigma_{OM}^2(h)),$ $\mu_{OM}(h) = q_1 \exp(q_2 h) + q_3 \exp(q_4 h);$ R-square = 0.9972 $q_1 = 4.449e - 06, q_2 = 1.38, q_3 = 0.08578, q_4 = -0.1565$ $\sigma_{OM}(h) = r_1 \exp(r_2 h) + r_3 \exp(r_4 h);$ R-square = 0.9991 $r_1 = -2.075e - 05, r_2 = 1.147, r_3 = 0.04924, r_4 = -0.1122$
Both LM and OM	$\Psi_{HI}(h) \sim \mathcal{N}(\mu_{HI}(h), \sigma_{HI}^2(h)),$ $\mu_{HI}(h) = m_1 \exp(m_2 h) + m_3 \exp(m_4 h);$ R-square = 0.9999 $m_1 = 2.498, m_2 = -2.243, m_3 = 0.1657, m_4 = -0.2552$ $\sigma_{HI}(h) = n_1 \exp(n_2 h) + n_3 \exp(n_4 h);$ R-square = 0.9921 $n_1 = 0.0633, n_2 = -0.233, n_3 = 2.153e - 06, n_4 = 1.529$

The data of rotational angle parameters along with the location of the UAV and the sensor node are used to estimate the deviation in elevation angle Ψ using (9). At each altitude, eighteen thousand samples of rotational angle (each for pitch, roll, and yaw) are collected, and deviation in elevation angle corresponding to them are estimated at each altitude. It has been observed that the deviation in elevation angle Ψ closely follows Gaussian shape for the data set at each height. For example, the histogram of Ψ at altitude $h = 1$ m is shown in Fig. 3(b). The mean and variance of the distribution of Ψ for each height is obtained and fitted using curve fitting technique in order to obtain the empirical equations as function of hovering altitude for analytical tractability, which are listed in Table I. Thus, Ψ at UAV hovering altitude h is modeled as

$$\Psi(h) \sim \mathcal{N}\left(\mu_{HI}(h), \sigma_{HI}^2(h)\right), \quad (10)$$

where \mathcal{N} denotes the Gaussian distribution; $\mu_{HI}(h)$ and $\sigma_{HI}(h)$ denote the mean and standard deviation, respectively, when the UAV hovers at altitude h .

The values of $\mu_{HI}(h)$ and $\sigma_{HI}(h)$ for different heights, e.g., 1 m to 5 m, are obtained by analyzing the distribution at each height. Next, the variation of $\mu_{HI}(h)$ and $\sigma_{HI}(h)$ against hovering altitude h are individually modeled through mathematically via curve fitting for analytical tractability. The modeled equations for $\mu_{HI}(h)$ and $\sigma_{HI}(h)$ along with the fitting coefficients are listed in Table I. The variation of the empirical and fitted values of mean $\mu_{HI}(h)$ and standard deviation $\sigma_{HI}(h)$ are respectively shown in Figs. 4(c) and 4(d), which indicate a good match. The R-square values are also listed in the table; the values close to 1 indicate the best fit.

Remark 4. For the scenario when the UAV experiences only OM, $\Phi_{LM} = 0$ and the distance between transmitter and receiver is equal to the hovering altitude. The above analysis will remain valid with $\Phi_{LM} = 0$ and the hovering inaccuracy parameters can be estimated. For this case,

the detailed analysis is not presented here for brevity, but the hovering inaccuracy parameters Ψ_{OM} , i.e., deviation in elevation angle due to OM-only is modeled and listed in Table I.

Remark 5. *The numerical analysis presented here is based on a data set of hovering inaccuracy measured using an experimental setup in Fig. 4(a). It is quite possible that the same UAV may exhibit different levels of hovering inaccuracy in different deployment scenarios and environmental conditions. However, the analytical framework and procedure to model the effect of hovering inaccuracy on system layout will remain the same as presented here in this work. Hence, it is important to estimate UAV hovering inaccuracy profile via a measurement campaign before facilitating RFET in a particular deployment scenario, and optimize the system parameters. UAV can also update the optimal system parameter in real-time according to the hovering profile.*

IV. ESTIMATION OF OPTIMAL SYSTEM PARAMETER

With the analysis and modeling of the hovering inaccuracy in the previous section, it is important to investigate the joint and individual impact of mismatches. These cases are important to analyze in order to evaluate the performance deviation due to the hovering inaccuracy and severity of each mismatch. For this purpose, four cases are considered as there are two types of mismatches, i.e., LM and OM, and the hovering inaccuracy is characterized in terms of the received power at the sensor node. Then the optimal system parameters, such as transmit power level, hovering altitude, and antenna parameter, are estimated. These parameters will play a key role in the UAV-aided RFET system design from practical deployment perspective.

A. Without Hovering Inaccuracy (Ideal Hovering)

In this case, the sensor node does not experience any hovering inaccuracy. This refers to the scenario when the UAV hovers vertically above the sensor node and does not undergo rotational motion. Thus, from (1), the received power at the sensor node when the UAV hovers at altitude h with N antenna elements mounted on it is obtained as

$$P_{rx}^{(Ideal)}(h, N) = P_{tx} \Lambda_0 F(\theta, \phi) \left(\frac{1}{d_{tx-rx}} \right)^2 \Bigg|_{d_{tx-rx}=h}^{\theta=0} = \frac{P_{tx} \Lambda_0 N}{h^2} = P_{tx} Z_{Ideal}(h, N), \quad (11)$$

where $Z_{Ideal}(h, N)$ is given as

$$Z_{Ideal}(h, N) = \Lambda_0 N / h^2. \quad (12)$$

Remark 6. $Z_{Ideal}(h, N)$ is not a convex function of h and N . It may be noted that, $Z_{Ideal}(h, N)$ is an increasing function of N for a given h . On the other hand, $Z_{Ideal}(h, N)$ is a decreasing function of h for a given N .

B. With Only Localization Mismatch (LM)

In this case, the sensor node experiences only LM. The UAV does not hover vertically above the sensor node as well as does not undergo rotational motion at this erroneous position. The beam is steered towards the ground node at angle $\Phi_{LM}(h)$ and the node is covered by a narrow beam. This leads to change in the distance between transmitter and receiver, but no deviation in the elevation angle is noted. Thus, from (1), the received power at the sensor node when the UAV hovers at altitude h with N antenna elements mounted on it is obtained as

$$P_{rx}^{(LM)}(h, N) = P_{tx}\Lambda_0 F(\theta, \phi) \left(\frac{1}{d_{tx-rx}} \right)^2 \Bigg|_{d_{tx-rx}=d(h)}^{\theta=0} = \frac{P_{tx}\Lambda_0 N}{[d(h)]^2} = P_{tx}Z_{LM}(h, N), \quad (13)$$

where $Z_{LM}(h, N)$ is given as

$$Z_{LM}(h, N) = \Lambda_0 N / [d(h)]^2. \quad (14)$$

Theorem 1. $Z_{LM}(h, N)$ is not proven to be a convex function of h and N .

Proof. See Appendix B. □

Lemma 1. $Z_{LM}(h, N)$ is a decreasing function of h for a given $N = N_0$.

Proof. See Appendix C. □

Lemma 2. $Z_{LM}(h, N)$ is an increasing function of N for a given $h = h_0$.

Proof. See Appendix D. □

$Z_{LM}(h, N)$ is not proven to a convex function of h and N , and therefore its variation against the individual parameters h and N are investigated. Lemma 1 reveals that $Z_{LM}(h, N = N_0)$ is a decreasing function of h , because the distance between transmitter and receiver increases with increase in h . Lemma 2 reveals that $Z_{LM}(h = h_0, N)$ is an increasing function of N , because the gain of antenna array mounted on UAV increases with increase in N . These observations are used helpful in estimating optimal system parameters.

C. With Only Orientation Mismatch (OM)

In this case, the sensor node experiences only OM. The UAV hovers vertically above the sensor node and undergoes rotational motion at this location. This does not change the distance between transmitter and receiver, but the deviation in the elevation angle is noted due to OM. Thus, from (1), the received power at the sensor node when the UAV hovers at altitude h with N antenna elements mounted on it is obtained as

$$P_{rx}^{(om)}(h, N) = P_{tx}\Lambda_0 F(\theta, \phi) \left(\frac{1}{d_{tx-rx}} \right)^2 \bigg|_{d_{tx-rx}=h}^{\theta \sim \Psi_{OM}(h)} = P_{tx}\Lambda_0 F(\theta, \phi) \frac{1}{h^2} \bigg|_{\theta \sim \Psi_{OM}(h)}. \quad (15)$$

It may be noted from Table I that the deviation in the elevation angle Ψ_{OM} is a random variable having Gaussian distribution. Hence, the received power in the expected sense is an appropriate metric for performance evaluation, because the UAV will have to hover for a long duration (up to a few minutes) in order to transfer several Joules of energy to each of the sensor nodes. Thus, the received power in the expected sense is evaluated as

$$P_{rx}^{(OM)}(h, N) = \mathbf{E} \left[P_{tx}\Lambda_0 F(\theta, \phi) \left(\frac{1}{h} \right)^2 \right] = P_{tx}\Lambda_0 \left(\frac{1}{h} \right)^2 \mathbf{E} [F(\theta, \phi)], \quad (16)$$

where $\mathbf{E}[\cdot]$ denotes the expectation operator.

The narrow beam pointed towards the sensor node gets displaced due to the hovering inaccuracy of the UAV, which leads to a deviation in the elevation angle. Thus, the sensor node does not lie within the beam transmitted by the antenna array mounted on the UAV. The gain of the directed beam is N when the sensor node is covered by it, whereas the gain is 0 when the sensor node is not covered by the beam. Therefore, $\mathbf{E}[F(\theta, \phi)]$ estimates the coverage of the sensor node, and to capture this a term named *coverage probability* $P_{cov}(h, N)$ is defined for analysis.

Definition 1. *The coverage probability refers to the possibility that the target sensor node lies within the beam spot generated by the UAV-mounted antenna array having N antenna elements hovering at altitude h .*

Using the definition 1 and the hovering parameters estimated in Table I, $P_{cov}^{(OM)}(h, N)$ is estimated as

$$P_{cov}^{(OM)}(h, N) = \Pr \left\{ -\frac{\theta_B(N)}{2} \leq \Psi_{OM}(h) \leq \frac{\theta_B(N)}{2} \right\} = Q \left(-\frac{\frac{\theta_B(N)}{2} - \mu_{OM}(h)}{\sigma_{OM}(h)} \right) - Q \left(\frac{\frac{\theta_B(N)}{2} + \mu_{OM}(h)}{\sigma_{OM}(h)} \right), \quad (17)$$

where $Q(\cdot)$ denotes the Gaussian Q-function.

Using the definition 1, $\mathbf{E}[F(\theta, \phi)]$ is given as

$$\mathbf{E}[F(\theta, \phi)] = NP_{cov}^{(OM)}(h, N). \quad (18)$$

Using the above finding, (16) is rewritten as

$$P_{rx}^{(OM)}(h, N) = P_{tx}\Lambda_0\left(\frac{1}{h}\right)^2 \mathbf{E}[F(\theta, \phi)] = P_{tx}\Lambda_0\left(\frac{1}{h}\right)^2 NP_{cov}^{(OM)}(h, N) = P_{tx}Z_{OM}(h, N), \quad (19)$$

where $Z_{OM}(h, N)$ is given as

$$Z_{OM}(h, N) = \Lambda_0 NP_{cov}^{(OM)}(h, N)/h^2. \quad (20)$$

It may be noted from (19) that the coverage probability depends on the variance of deviation in elevation angle; increase in variance leads to decrease in coverage probability and vice versa. Thus, the variance of deviation in elevation angle has strong impact on received power at the sensor node, because the received power is directly proportional to the coverage probability.

Theorem 2. $Z_{OM}(h, N)$ is not proven to be a convex function of h and N .

Proof. See Appendix E. □

Lemma 3. $Z_{OM}(h, N)$ is an increasing function of h for a given $N = N_0$.

Proof. See Appendix F. □

Lemma 4. $Z_{OM}(h, N)$ is an increasing function of N for a given $h = h_0$.

Proof. See Appendix G. □

The variation of $Z_{OM}(h, N)$ against the individual parameters h and N , is investigated, as it is not proven to be a convex function of h and N . Lemma 3 suggests that $Z_{OM}(h, N = N_0)$ is a decreasing function of h . This happens, because the distance between transmitter and receiver increases with increase in altitude. In addition, the coverage probability also decreases with altitude, as the mean and variance of deviation in elevation angle Ψ_{OM} decreases with increase in altitude. Lemma 4 reveals that $Z_{OM}(h = h_0, N)$ is an increasing function of N . The gain of antenna array increases with increase in N , whereas the coverage probability decreases with increase in N due to reduced HPBW. $Z_{OM}(h = h_0, N)$ is the product of antenna gain and coverage probability. The increase in antenna gain overcomes the effect of reduction in coverage probability, and as a result $Z_{OM}(h = h_0, N)$ increases with increase in N .

D. With Both LM and OM

In this case, the UAV does not hover vertically above the sensor node (i.e., LM), which leads to a change in the distance between transmitter and receiver. In addition, the UAV undergoes rotational motion at this erroneous position (i.e., OM), which leads to a deviation in the elevation angle between transmitter and receiver. Thus, from (1), the received power at the sensor node when the UAV hovers at altitude h with N antenna elements mounted on it is obtained as

$$P_{rx}^{(hi)}(h, N) = P_{tx}\Lambda_0 F(\theta, \phi) \left(\frac{1}{d_{tx-rx}} \right)^2 \Bigg|_{d_{tx-rx}=d(h)}^{\theta \sim \Psi_{HI}(h)} = P_{tx}\Lambda_0 F(\theta, \phi) \left(\frac{1}{d(h)} \right)^2 \Bigg|_{\theta \sim \Psi_{HI}(h)}. \quad (21)$$

It may be noted from (10) that the deviation in the elevation angle θ is a random variable having Gaussian distribution. The received power in the expected sense is evaluated as

$$P_{rx}^{(HI)}(h, N) = \mathbf{E}[P_{rx}^{(hi)}(h, N)] = \mathbf{E} \left[\frac{P_{tx}\Lambda_0}{[d(h)]^2} F(\theta, \phi) \right] = \frac{P_{tx}\Lambda_0}{[d(h)]^2} \mathbf{E}[F(\theta, \phi)]. \quad (22)$$

By definition 1 and the estimated parameters in Table I, $P_{cov}^{(HI)}(h, N)$ is estimated as

$$P_{cov}^{(HI)}(h, N) = \Pr \left\{ -\frac{\theta_B(N)}{2} \leq \Psi_{HI}(h) \leq \frac{\theta_B(N)}{2} \right\} = \mathbf{Q} \left(-\frac{\frac{\theta_B(N)}{2} - \mu_{HI}(h)}{\sigma_{HI}(h)} \right) - \mathbf{Q} \left(\frac{\frac{\theta_B(N)}{2} + \mu_{HI}(h)}{\sigma_{HI}(h)} \right). \quad (23)$$

Now, $\mathbf{E}[F(\theta, \phi)]$ is estimated as

$$\mathbf{E}[F(\theta, \phi)] = NP_{cov}^{(HI)}(h, N). \quad (24)$$

Using the above finding, (22) is rewritten as

$$P_{rx}^{(HI)}(h, N) = \frac{P_{tx}\Lambda_0}{[d(h)]^2} \mathbf{E}[F(\theta, \phi)] = \frac{P_{tx}\Lambda_0 NP_{cov}^{(HI)}(h, N)}{[d(h)]^2} = P_{tx}Z_{HI}(h, N), \quad (25)$$

where $Z_{HI}(h, N)$ is given as

$$Z_{HI}(h, N) = \Lambda_0 NP_{cov}^{(HI)}(h, N)/[d(h)]^2. \quad (26)$$

Theorem 3. $Z_{HI}(h, N)$ is not proven to be a convex function of h and N .

Proof. See Appendix H. □

Lemma 5. $Z_{HI}(h, N)$ is a unimodal function of h for a given $N = N_0$.

Proof. See Appendix I. □

Lemma 6. $Z_{HI}(h, N)$ is a unimodal function of N for a given $h = h_0$.

Proof. See Appendix J. □

Lemma 5 reveals the unimodal nature of $Z_{HI}(h, N = N_0)$. The coverage probability increases with increase in h due to decrease in mean and variance of Φ_{HI} and the distance between transmitter and receiver increases at the same time. Thus, at a lower altitude, reduction in coverage probability dominates due to significantly higher values of mean and variance of Φ_{HI} , whereas the distance between transmitter and receiver dominates at a higher altitude. Therefore, $Z_{HI}(h, N = N_0)$ exhibits unimodal variation against h . Lemma 6 reveals the unimodal variation of $Z_{HI}(h = h_0, N)$. The HPBW reduces with increase in N and the gain of antenna array increases at the same time. The coverage probability decreases with increase in N due to reduction in HPBW. Therefore, $Z_{HI}(h = h_0, N)$ exhibits unimodal variation. It may be noted from Table I that the magnitude of mean and variance of Ψ_{OM} is significantly lesser than that of Ψ_{HI} . Due to this, Lemmas 3 and 4 exhibit different characteristics than Lemmas 5 and 6.

E. Estimation of Optimal System Parameters

Till now, the received power level at the sensor node for all the four cases have been obtained, which will be used to estimate the optimal system parameters. For this purpose, an optimization problem to obtain the optimal system parameters for the k^{th} case is formulated as

$$\text{(P1)} : \underset{h, N}{\text{minimize}} \quad P_{tx}^{(k)}, \quad k = \{\text{Ideal, LM, OM, HI}\} \quad (27)$$

$$\text{s. t.: (C1)} : \mathbf{E}[P_{rx}^{(k)}(h, N)] \geq P_o, \quad \text{(C2)} : h_{min} \leq h \leq h_{max}, \quad \text{(C3)} : N_{min} \leq N \leq N_{max}.$$

The objective function of **(P1)** ensures the transfer of at least P_o amount of power to the ground deployed sensor node by radiating minimum amount of power from the UAV-mounted transmitter. Towards this, the objective function aims to select the appropriate hovering altitude and the antenna parameters so that the transmitted power level can be minimized in order to receive a power level higher than P_o . Constraint **(C1)** captures the received power threshold characteristics. Constraint **(C2)** restricts the UAV hovering altitude range, whereas constraint **(C3)** limits the range of the number of antenna elements mounted on the UAV.

Using (11), (13), (16), and (25), constraint **(C1)** is rewritten as

$$\mathbf{E}[P_{rx}^{(k)}(h, N)] \geq P_o \Rightarrow P_{tx}^{(k)} \cdot Z_k(h, N) \Rightarrow P_{tx}^{(k)} \geq \frac{P_o}{Z_k(h, N)}, \quad k = \{\text{Ideal, LM, OM, HI}\}. \quad (28)$$

Using (28), the optimization problem **(P1)** is rewritten as

$$\text{(P2)} : \underset{h, N}{\text{maximize}} \quad Z_k(h, N), \quad k = \{\text{Ideal, LM, OM, HI}\}; \quad \text{s. t.: (C2) and (C3)} \quad (29)$$

Thus, the optimization problem **(P1)** is transformed into **(P2)** and solving **(P2)** is equivalent to solving **(P1)**. Moreover, Remark 6, Theorems 1 through 3 indicate that $Z_k(h, N)$ is not a convex function of h and N . Therefore, numerical techniques are needed to solve this optimization problem, where the characteristics of $Z_k(h, N)$ proved in Lemmas 1 through 6 will be explored. For the ideal case without hovering inaccuracy $Z_k(h, N)$ with $k = \{\text{Ideal}\}$, the minimum hovering altitude is the optimal one, whereas the maximum allowable value of N is the optimal one (see Remark 6). On one hand, for LM-only and OM-only cases, the optimal hovering altitude is the lowest possible one, i.e., h_{min} (see Lemmas 1 and 3), and the optimal number of antenna elements is the maximum allowable one, i.e., $N = N_{max}$ (see Lemmas 2 and 4). On the other hand, in presence of both LM and OM, $Z_k(h, N)$ with $k = \{\text{HI}\}$ exhibits unimodal variation against h for a given N (see Lemma 5). Also, $Z_k(h, N)$ with $k = \{\text{HI}\}$ exhibits unimodal variation against N for a given h (see Lemma 6). Using the characteristics of the received power, an algorithm is proposed (Algorithm 1) to estimate the values of optimal system parameters with both LM and OM. Here, the optimal hovering altitude, which is the root of $\frac{\partial}{\partial h} Z_{HI}(h, N_0) = 0$, is obtained using bisection method for a given number of antenna elements. Then $Z_{HI}(\cdot, \cdot)$ is calculated and compared with the previous set of optimal value. This process is repeated until decrease in $Z_{HI}(\cdot, \cdot)$ is noted due to unimodal variation of $Z_{HI}(h, N)$ against h and N individually. The computational complexity of Algorithm 1 is $\mathcal{O}(h_{max}N_{max})$, because the computational complexity of bisection method depends on the search interval and accuracy of the solution (a constant, which is taken as 0.01 m). The variation of the function evolved in the optimization problem is characterized in Lemma 5 and Lemma 6, and found to exhibit unimodal variation. It may be noted that the unimodal function contains a unique optimal in the domain of definition, which ensures the convergence of Algorithm 1 in finite iteration. Further, the optimal solution estimated by Algorithm 1 is a global optimal solution due to presence of unique optimal in unimodal function.

V. RESULTS AND DISCUSSIONS

Numerical evaluation of the analyses in Sections III and IV is presented here. The hovering inaccuracy parameters in Table I are used in simulations. The system parameter values considered are: $P_{tx} = 1 \text{ W}$, $G_{rx} = 2.10$, $f_c = 28 \text{ GHz}$, $N_{min} = 1$, $N_{max} = 150$, $h_{min} = 1 \text{ m}$, $h_{max} = 5 \text{ m}$.

A. Effect of Coverage Probability

Algorithm 1 Estimation of Optimal System Parameters

- 1: **Input:** $\Lambda_0, N_{min}, N_{max}, h_{min}, h_{max}, P_0$, hovering inaccuracy parameters (Table I and (9))
 - 2: **Output:** $P_{tx}^{opt}, h_{opt}, N_{opt}$
 - 3: $\epsilon = 0.01, N_0 = N_{min}$
 - 4: Find $h_r(N_0)$, the root of $\frac{\partial}{\partial h} Z_{HI}(h, N_0) = 0$ (see Appendix I), using bisection method
 - 5: Calculate $Z_{HI}(h_r(N_0), N_0)$ (see (26))
 - 6: **while** $\epsilon \geq 0$ **do**
 - 7: $N_0 = N_0 + 1,$
 - 8: Find $h_r(N_0)$, the root of $\frac{\partial}{\partial h} Z_{HI}(h, N_0) = 0$, using bisection method
 - 9: Calculate $Z_{HI}(h_r(N_0), N_0), \epsilon = Z_{HI}(h_r(N_0), N_0) - Z_{HI}(h_r(N_0 - 1), N_0 - 1)$
 - 10: **end**
 - 11: $n_{opt} = N_0 - 1, h_{opt} = h_r(N_0 - 1), P_{tx}^{opt} = [P_0]/[\Lambda_0 \cdot Z_{HI}(h_{opt}, n_{opt})]$
-

The variation of coverage probability against the number of antenna elements N at different hovering altitudes for the two cases (OM-only and both LM and OM) is shown in Fig. 5, where the hovering inaccuracy occurs due to the rotational motion of the UAV. It can be observed that the coverage probability decreases with increase in N due to decrease in the HPBW, which leads to a reduced size of the beam spot wherein the sensor node cannot be covered. Moreover, $P_{cov}(h, N)$ increases with hovering altitude, because the mean and standard deviation of the deviation in elevation angle (see $\Psi_{OM}(h)$ and $\Psi_{HI}(h)$ in Table I) decreases with increase in hovering altitude. Hence, the antenna's beam does not get displaced significantly at higher hovering altitude, which ensures coverage of the sensor node within the beam spot. The effect of coverage probability is more severe in the case of both LM and OM as compared to OM-only. This is because the UAV hovers vertically above the sensor node in OM-only case. This leads to symmetric radiation pattern of antenna's beam about the vertical axis in this orientation, where the effect of the *yaw* is not severe. On the other hand, the antenna beam is directed towards the distant located sensor node in case of both LM and OM. This leads to asymmetric radiation pattern of the beam about the vertical axis in this orientation, where the rotation along the *yaw* results in significant deviation in elevation angle.

Remark 7. *Hovering inaccuracy of UAV leads to reduce the effective gain of antenna beam directed towards the sensor node, which has strong impact on the performance.*

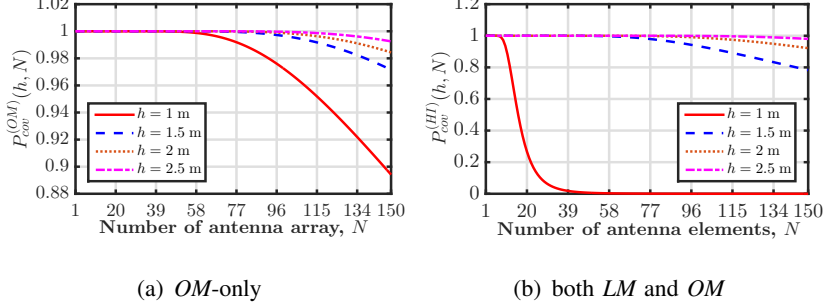


Figure 5: Variation of $P_{cov}(h, N)$ against number of antenna elements for different cases.

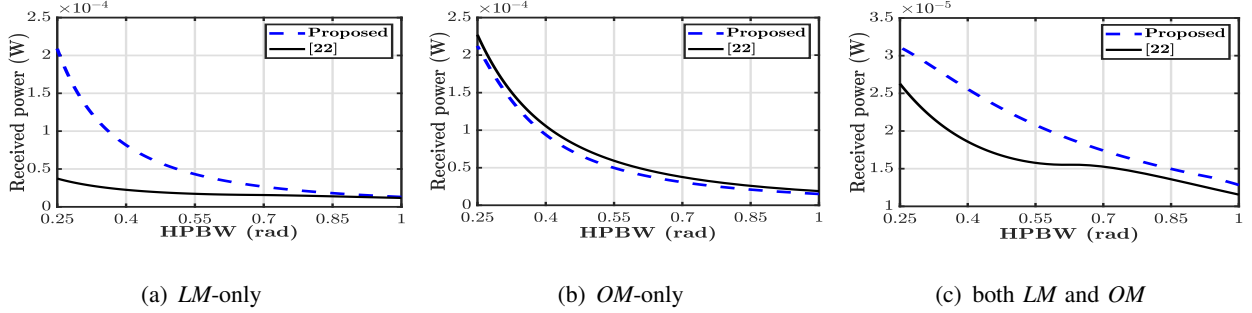


Figure 6: Variation of optimal received power against HPBW for different cases of mismatch with $P_{tx} = 1$ W.

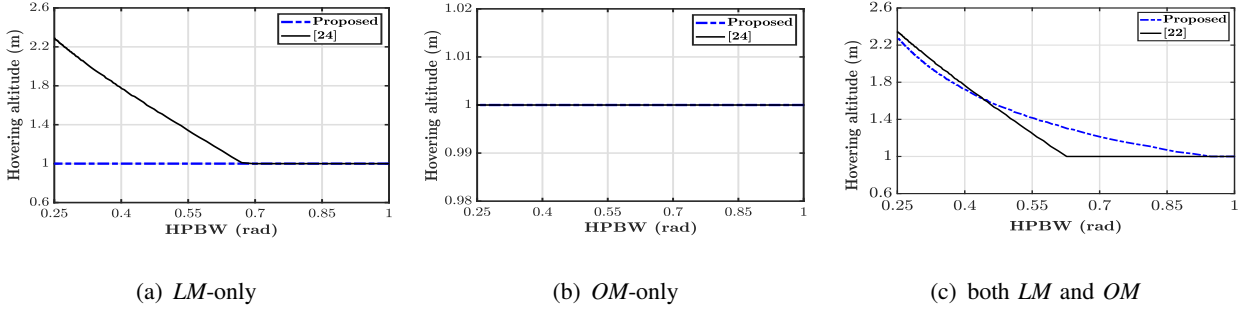


Figure 7: Variation of optimal hovering altitude against HPBW to receive optimal power level for different cases for proposed framework and the work reported in [22] with $P_{tx} = 1$ W.

B. Comparison of Hovering Inaccuracy Mitigation Performance

The work reported in prior art [22] is considered for comparison purpose. The radiation pattern of transmitter antenna mounted on the UAV is: $g(n, \theta) = 2(n+1) \cos^n(\theta)$, where n is the antenna exponent and θ is the elevation angle between transmitter and receiver. The HPBW of this antenna is $\sqrt{2\pi/(n+1)}$. This directional antenna has a symmetrical radiation pattern about the vertical axis as opposed to the narrow beam having an asymmetric radiation pattern considered here in this work. To demonstrate the mitigation capability of the proposed framework, variation of the received power against HPBW is shown in Fig. 6 for different cases. The transmit power level is considered to be 1 W and the dimension of the antenna array depends upon the HPBW value. Then, the UAV optimizes its hovering altitude (as shown in Fig. 7) so that the maximum power

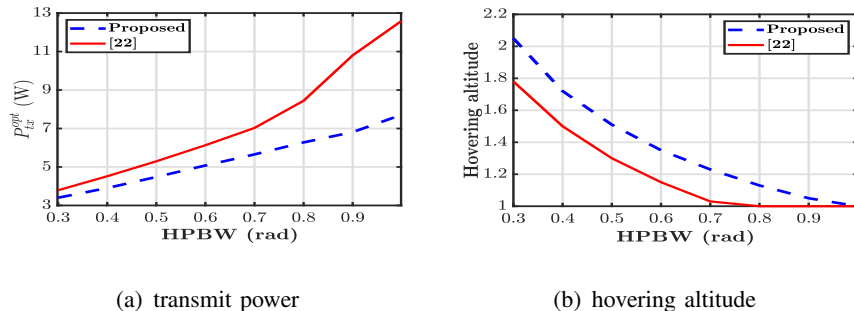


Figure 8: Comparison of optimal (a) transmit power and (b) hovering altitude against HPBW for $P_o = 0.1$ W.

can be received at the sensor node. Fig. 6(a) reveals that LM-only case, the received power level in the proposed framework is much higher than the prior art. However, the gap reduces and the received power level is almost same for both of the methods as HPBW increases. This happens because the narrow beam offers much higher gain, which overcomes the loss due to LM significantly in the proposed beam steering based framework. Besides, the loss caused by coverage probability is not here due to the absence of rotation motion of UAV. The optimal UAV hovering altitude variation for this case shown in Fig. 7(b) indicates that the UAV hovers at the lowest allowable altitude in the proposed framework, whereas the UAV needs to hover at a higher altitude to overcome LM without beam steering, as considered in [22]. For OM-only case where there is no LM, Fig. 6(b) indicates that the received power level in the proposed framework is slightly less than that in [22]. This is caused due to reduction in the effective gain of antenna's beam due to coverage probability (see Fig. 5(a)). Although the gap is nominal, it reveals that the effect of OM in the proposed beam steering based RFET framework is more severe than that in [22]. However, the optimal hovering altitude is the same and the lowest allowable altitude for both as shown in Fig. 7(b). With both LM and OM, the received power level variation against HPBW is shown in Fig. 6(c), which reveals that the received power level in the proposed framework is much higher than [22]. Optimal altitude variation against HPBW shown in Fig. 7(c) indicates that the UAV hovers at higher altitude for smaller values of HPBW, which offers a larger beam spot on the ground to ensure the node's coverage.

Variation of the optimal transmit power level required to achieve the objectives of the optimization problem **(P1)** against HPBW is shown in Fig. 8(a) for the proposed method and [22]. One can observe that relatively less power needs to be transmitted in the proposed framework as compared to the same in prior art. The saving in transmit power level up to 36% is observed. To meet this performance, the UAV hovers at a higher altitude in the proposed framework as compared

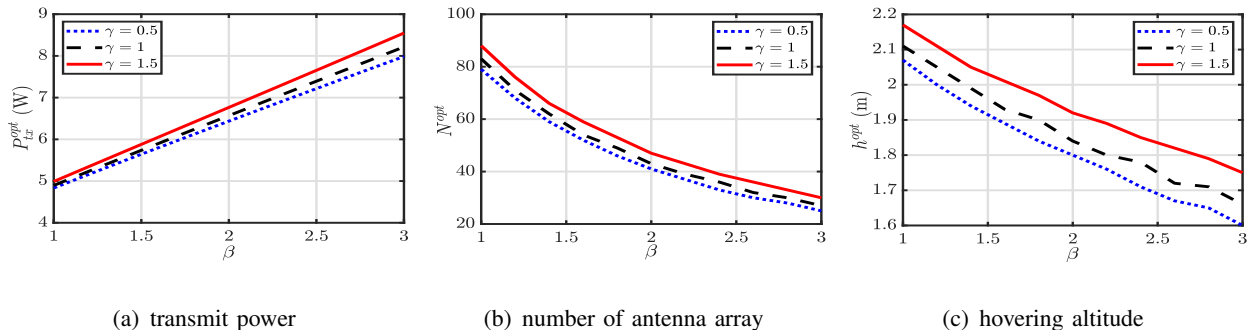


Figure 9: Variation of optimal system parameters for different level of hovering inaccuracy for $P_o = 0.1$ mW.

to that in prior art as shown in Fig. 8(b). The discussion made above reveals that the proposed mitigation framework is energy-efficient and overcomes the effect of hovering inaccuracy, as relatively less transmit power needs to be transmitted to achieve the same performance.

Remark 8. *The proposed beam steering based framework treats LM and OM very differently. It mitigates LM effectively, whereas OM exhibits adverse effect. However, an overall gain in performance improvement is noticed by jointly accounting for both the mismatches.*

C. Impact of Varying Hovering Inaccuracy

The analysis presented till now is based on the parameters listed in Table I, which had been estimated using the data collected by conducting experiments in an open space (hockey ground). This can be thought of as an ideal deployment scenario, because GPS signals from nine satellites were available. It is quite possible that the UAV may experience different levels of hovering inaccuracy in different deployment scenarios while facilitating UAV-aided RFET, where the amount of LM and OM can be much higher than that obtained in Table I. It is important to investigate the mitigation capability of the proposed framework in such a deployment scenario having varying level of hovering inaccuracy. To this end, to model the severity of the hovering inaccuracy, we have used two tuning parameters $\gamma > 0$ and $\beta > 0$ to capture the variation in distance and the deviation in elevation angle, respectively.

The γ -dependent distance between transmitter and receiver is formulated as

$$d_{(\gamma)}(h) = \sqrt{h^2 + (\gamma|O_u O_s|)^2} \quad \text{with} \quad |O_u O_s| = \sqrt{[d(h)]^2 - h^2}. \quad (30)$$

Here, the increase in horizontal distance between the sensor node (O_s) and the ground projection of the UAV (O_u), i.e., $|O_u O_s|$, depicts the GPS error (see Fig. 2), whereas γ indicates the severity of LM. $\gamma > 1$ indicates that the amount of LM is higher than that in Table I, whereas $0 < \gamma < 1$

indicates that the amount of LM is less than that in Table I. The β -dependent deviation in elevation angle is formulated as $\Psi_{(\beta)}(h) \sim \mathcal{N}(\mu_{HI}(h), \sigma_{HI}^2(h)) + \beta \cdot \mu_0$, where $\mu_0 = 0.03$ is the additional deviation in elevation angle. This indicates that the UAV undergoes severe rotation motion along *pitch*, *roll*, and *yaw*, which leads to a higher deviation in elevation angle.

Now, the received power level is obtained from (25) using the distance between transmitter and receiver $d_{(\gamma)}(h)$ and the deviation in elevation angle $\Psi_{(\beta)}(h)$. The characteristics of the received power for this case has been investigated, which exhibits same variation as proved in Theorem 3, Lemma 5, and Lemma 6. Thus, the optimal system parameters can be evaluated using Algorithm 1. The optimal system parameters for the ideal case without any hovering inaccuracy is: $(P_{tx}^{opt}, h_{opt}, N_{opt})|_{\text{Ideal}} = (0.44 \text{ W}, 1 \text{ m}, 150)$. On the other hand, the variation of the optimal system parameters against severity of OM for different level of LM is shown in Fig. 9. One can observe from Fig. 9(a) that it requires to transmit significantly higher power level as the amount of OM increases. Furthermore, the optimal number of antenna elements reduces as β increases as shown in Fig. 9(b), because a lower value of N offers a higher HPBW which ensures the coverage of the sensor node within the beam spot. The optimal hovering altitude also decreases with increase in β as shown in Fig. 9(c) to balance the loss due to coverage probability which reduces with β . It is also noted from Fig. 9 that the effect of different level of OM is more severe than that of LM, because the variation in the optimal system parameters is not significant when amount of LM increases. However, the proposed framework offers overall performance gain by mitigating the effect of both LM and OM.

VI. CONCLUDING REMARKS

An antenna beam steering based mitigation strategy to reduce the effect of hovering inaccuracy in the performance of UAV-aided RFET has been presented. A narrow beam is transmitted towards the ground sensor node from the antenna array mounted on the bottom of the UAV. The center of the narrow beam is displaced due to hovering inaccuracy, which leads to an uncertain ground coverage by the transmitted beam. An analytical framework to estimate the deviation in elevation angle has been presented and its parameters have been evaluated using data collected from the UAV-based experimental setup. With this finding, closed-form expressions for the received power at the ground sensor node have been obtained for the ideal hovering condition of the UAV and in the presence of hovering inaccuracy of the UAV. The nature of variation of the received power has also been characterized. Then, an optimization problem has been formulated

to evaluate the optimal values of system parameters, i.e., transmit power level, hovering altitude, and antenna parameter. This problem has been proven to be a nonconvex optimization problem, and an algorithm is proposed to solve this. Performance analysis and simulation results reveal that the proposed framework is found to be more energy-efficient in mitigating hovering inaccuracy, as the same performance can be achieved with less transmit power level (up to 36%) as compared to the prior art. The proposed framework also mitigates the varying level of hovering inaccuracy.

Further investigations on the study of charging mechanism with multi-UAV deployment scenario in presence of hovering inaccuracy would be of future research interest, where mapping of nodes to appropriate UAV, trajectory optimization of each of the UAVs, and estimation of charging time required by each node will be of major concern, while accounting for the energy constraint of UAVs. While the analysis of LM and OM in this paper generically captures the UAV hovering inaccuracy, an interesting direction would be exclusive investigation on the effects of environmental factors, such as wind and fog, on the hovering inaccuracy and performance of UAV-aided RFET. The effect of UAV orientation mismatch due to pitch, roll, and yaw is also very interesting and challenging issue when the UAV communicates using beamforming with another UAV or base station over the backhaul data link.

APPENDIX

A. Proof of Theorem 2

For convenience, let us assume that

$$D(h) = d^2(h), \quad D'(h) = \frac{\partial}{\partial h} D(h) = 2u_1 h + u_2, \quad D''(h) = 2u_1 \quad (\text{see 9}). \quad (\text{B-1})$$

The Hessian matrix $Z_{LM}(h, N)$ is obtained as: $\mathcal{H}_{LM}(h, N) = \begin{bmatrix} \frac{\partial^2 Z_{LM}(h, N)}{\partial h^2} & \frac{\partial^2 Z_{LM}(h, N)}{\partial h \partial N} \\ \frac{\partial^2 Z_{LM}(h, N)}{\partial N \partial h} & \frac{\partial^2 Z_{LM}(h, N)}{\partial N^2} \end{bmatrix} = \Lambda_0 \begin{bmatrix} \frac{2D(h)[D'(h)]^2 - [D(h)]^2 D''(h)}{[D(h)]^4} & -\frac{D'(h)}{[D(h)]^2} \\ -\frac{D'(h)}{[D(h)]^2} & 0 \end{bmatrix}$. The determinant of $\mathcal{H}_{LM}(h, N)$ is $|\mathcal{H}_{LM}(h, N)| = -\left(\Lambda_0 \frac{D'(h)}{[D(h)]^2}\right)^2$, which is negative and hence $Z_{LM}(h, N)$ is not a convex function of h and N .

B. Proof of Lemma 1

The derivative of $Z_{LM}(h, N)$ with respect to h for a given value of $N = N_0$ is obtained as: $\frac{\partial}{\partial h} Z_{LM}(h, N_0) = -\Lambda_0 N_0 \frac{D'(h)}{[D(h)]^2}$. From the parameters listed in Table I, one can deduce that $D'(h) > 0 \forall h$. Hence, $\frac{\partial}{\partial h} Z_{LM}(h, N_0) < 0 \forall h$, which proves the decreasing nature of $Z_{LM}(h, N_0)$ against h .

C. Proof of Lemma 2

The derivative of $Z_{LM}(h, N)$ with respect to N for a given value of $h = h_0$ is: $\frac{\partial}{\partial N} Z_{LM}(h_0, N) = \Lambda_0 \frac{1}{D(h_0)}$. From the parameters listed in Table I, one can deduce that $D(h) > 0 \forall h$. Hence, $\frac{\partial}{\partial N} Z_{LM}(h_0, N) > 0 \forall N$, which proves the increasing nature of $Z_{LM}(h_0, N)$ against N .

D. Proof of Theorem 3

For convenience, let us denote

$$V(h, N) = -\frac{\frac{\theta_B(N)}{2} - \mu_{OM}(h)}{\sigma_{OM}(h)}, \quad W(h, N) = \frac{\frac{\theta_B(N)}{2} + \mu_{OM}(h)}{\sigma_{OM}(h)}. \quad (\text{E-1})$$

The derivatives of $V(h, N)$ with respect to h and N are obtained as

$$\begin{aligned} V_h(h, N) &= \frac{\partial}{\partial h} V(h, N) = \frac{\partial}{\partial h} \left(\frac{\mu_{OM}(h) - \frac{\pi}{2\sqrt{N}}}{\sigma_{OM}(h)} \right) = \frac{\sigma_{OM}(h)\mu'_{OM}(h) - (\mu_{OM}(h) - \frac{\pi}{2\sqrt{N}})\sigma'_{OM}(h)}{[\sigma_{OM}(h)]^2}, \\ V_N(h, N) &= \frac{\partial}{\partial N} V(h, N) = \frac{\pi}{4\sigma_{OM}(h)} N^{-3/2}, \\ V_{hh}(h, N) &= \frac{\partial^2}{\partial h^2} V(h, N) = \frac{\sigma_{OM}^2(h)[\sigma_{OM}(h)\mu''_{OM}(h) - \sigma''_{OM}(h)(\mu_{OM}(h) - \frac{\pi}{2\sqrt{N}})] - 2\sigma_{OM}(h)\sigma'_{OM}(h)[\sigma_{OM}(h)\mu'_{OM}(h) - (\mu_{OM}(h) - \frac{\pi}{2\sqrt{N}})\sigma_{OM}(h)]}{[\sigma_{OM}(h)]^4}, \\ V_{Nh}(h, N) &= V_{hN}(h, N) = \frac{\partial^2}{\partial N \partial h} V(h, N) = -\frac{\pi}{4} \frac{\sigma'_{OM}(h)}{\sigma_{OM}^2(h)} N^{-3/2}, \\ V_{NN}(h, N) &= \frac{\partial^2}{\partial N^2} V(h, N) = -\frac{3\pi}{8\sigma_{OM}(h)} N^{-5/2}, \end{aligned} \quad (\text{E-2})$$

where $\mu'_{OM}(h) = \frac{\partial}{\partial h} \mu_{OM}(h)$, $\sigma'_{OM}(h) = \frac{\partial}{\partial h} \sigma_{OM}(h)$, $\mu''_{OM}(h) = \frac{\partial^2}{\partial h^2} \mu_{OM}(h)$, $\sigma''_{OM}(h) = \frac{\partial^2}{\partial h^2} \sigma_{OM}(h)$.

The derivatives of $W(h, N)$ with respect to h and N are obtained as

$$\begin{aligned} W_h(h, N) &= \frac{\partial}{\partial h} W(h, N) = \frac{\partial}{\partial h} \left(\frac{\mu_{OM}(h) + \frac{\pi}{2\sqrt{N}}}{\sigma_{OM}(h)} \right) = \frac{(\mu_{OM}(h) + \frac{\pi}{2\sqrt{N}})\sigma'_{OM}(h) - \sigma_{OM}(h)\mu'_{OM}(h)}{[\sigma_{OM}(h)]^2}, \\ W_N(h, N) &= \frac{\partial}{\partial N} W(h, N) = -\frac{\pi}{4\sigma_{OM}(h)} N^{-3/2}, \\ W_{hh}(h, N) &= \frac{\partial^2}{\partial h^2} W(h, N) = \frac{\sigma_{OM}^2(h)[\sigma'_{OM}(h)(\mu_{OM}(h) + \frac{\pi}{2\sqrt{N}}) - \sigma_{OM}(h)\mu''_{OM}(h)] - 2\sigma_{OM}(h)\sigma'_{OM}(h)[(\mu_{OM}(h) + \frac{\pi}{2\sqrt{N}})\sigma'_{OM}(h) - \sigma_{OM}(h)\mu'_{OM}(h)]}{[\sigma_{OM}(h)]^4}, \\ W_{Nh}(h, N) &= W_{hN}(h, N) = \frac{\partial^2}{\partial N \partial h} W(h, N) = \frac{\pi}{4} \frac{\sigma'_{OM}(h)}{\sigma_{OM}^2(h)} N^{-3/2}, \\ W_{NN}(h, N) &= \frac{\partial^2}{\partial N^2} W(h, N) = \frac{3\pi}{8\sigma_{OM}(h)} N^{-5/2}. \end{aligned} \quad (\text{E-3})$$

Using (E-1) and (E-2), the derivatives of $Q(U(h, N))$ with respect to h and N are obtained as

$$\begin{aligned} Q_h(V(h, N)) &= \frac{\partial Q(V(h, N))}{\partial h} = -\frac{1}{2\pi} \exp(-[V(h, N)]^2/2) V_h(h, N), \\ Q_N(V(h, N)) &= \frac{\partial Q(V(h, N))}{\partial N} = -\frac{1}{2\pi} \exp(-[V(h, N)]^2/2) V_N(h, N), \end{aligned}$$

$$\begin{aligned}
Q_{hh}(V(h, N)) &= \frac{\partial^2 Q(V(h, N))}{\partial h^2} = \frac{1}{2\pi} \exp(-[V(h, N)]^2/2) [V(h, N)(V_h(h, N))^2 - V_{hh}(h, N)], \quad (\text{E-4}) \\
Q_{NN}(V(h, N)) &= \frac{\partial^2 Q(V(h, N))}{\partial N^2} = \frac{1}{2\pi} \exp(-[V(h, N)]^2/2) [V(h, N)(V_N(h, N))^2 - V_{NN}(h, N)], \\
Q_{hN}(V(h, N)) &= Q_{Nh}(V(h, N)) = \frac{\partial^2 Q(V(h, N))}{\partial h \partial N} = \frac{1}{2\pi} \exp(-[V(h, N)]^2/2) [V(h, N)V_h(h, N)V_N(h, N) - V_{hN}(h, N)].
\end{aligned}$$

Using (17) and (E-4), the derivatives of $P_{cov}(h, N)$ are obtained as

$$\begin{aligned}
{}_h P_{cov}^{(OM)}(h, N) &= \frac{\partial}{\partial h} P_{cov}^{(OM)}(h, N) = Q_h(V(h, N)) - Q_h(W(h, N)), \\
{}_N P_{cov}^{(OM)}(h, N) &= \frac{\partial}{\partial N} P_{cov}^{(OM)}(h, N) = Q_N(V(h, N)) - Q_N(W(h, N)), \\
{}_{hh} P_{cov}^{(OM)}(h, N) &= \frac{\partial^2}{\partial h^2} P_{cov}^{(OM)}(h, N) = Q_{hh}(V(h, N)) - Q_{hh}(W(h, N)), \quad (\text{E-5}) \\
{}_{NN} P_{cov}^{(OM)}(h, N) &= \frac{\partial^2}{\partial N^2} P_{cov}^{(OM)}(h, N) = Q_{NN}(V(h, N)) - Q_{NN}(W(h, N)), \\
{}_{hN} P_{cov}^{(OM)}(h, N) &= {}_{Nh} P_{cov}^{(OM)}(h, N) = \frac{\partial^2}{\partial h \partial N} P_{cov}^{(OM)}(h, N) = Q_{hN}(V(h, N)) - Q_{hN}(W(h, N)).
\end{aligned}$$

In the same way, the derivatives of $Q(W(h, N))$ with respect to h and N can be obtained using E-2, E-3, and (E-4).

Now, the Hessian matrix of $Z_{OM}(h, N)$ is given as

$$\mathcal{H}_{OM}(h, N) = \begin{bmatrix} \frac{\partial^2 Z_{OM}(h, N)}{\partial h^2} & \frac{\partial^2 Z_{OM}(h, N)}{\partial h \partial N} \\ \frac{\partial^2 Z_{OM}(h, N)}{\partial N \partial h} & \frac{\partial^2 Z_{OM}(h, N)}{\partial N^2} \end{bmatrix} = \Lambda_0 \begin{bmatrix} \kappa_{11} & \kappa_{12} \\ \kappa_{21} & \kappa_{22} \end{bmatrix}.$$

Using (B-1) and (E-5), the elements of the Hessian matrix $\mathcal{H}_{OM}(h, N)$ are obtained as

$$\begin{aligned}
\kappa_{11} &= N \frac{[D(h)]^2 [D(h) {}_{hh} P_{cov}^{(OM)}(h, N) - P_{cov}^{(OM)}(h, N) D''(h) - 2D'(h) {}_h P_{cov}^{(OM)}(h, N)] + 2[D'(h)]^2 P_{cov}^{(OM)}(h, N) D(h)}{[D(h)]^4}, \\
\kappa_{12} = \kappa_{21} &= \frac{D(h) [{}_h P_{cov}^{(OM)}(h, N) + N {}_{Nh} P_{cov}^{(OM)}(h, N)] - D'(h) [P_{cov}^{(OM)}(h, N) + N {}_N P_{cov}^{(OM)}(h, N)]}{[D(h)]^2}, \\
\kappa_{22} &= \frac{2{}_N P_{cov}^{(OM)}(h, N) + N {}_{NN} P_{cov}^{(OM)}(h, N)}{D(h)}, \quad (Z_{OM}(h, N) \text{ is continuous, hence } \kappa_{12} = \kappa_{21}).
\end{aligned}$$

For a function to be convex, the Hessian matrix should be positive semidefinite. The variation of the eigenvalues of $|\mathcal{H}_{OM}(h, N)|$ against h and N is shown in Fig. 10 (a) and (b). The presence of eigenvalues of opposite sign ensures that $\mathcal{H}_{OM}(h, N)$ is not a convex function of h and N .

E. Proof of Lemma 3

The derivative of $Z_{OM}(h, N)$ with respect to h for a given value of $N = N_0$ is obtained as

$$\frac{\partial}{\partial h} Z_{OM}(h, N_0) = N_0 \frac{D(h) {}_h P_{cov}^{(OM)}(h, N_0) - D'(h) P_{cov}^{(OM)}(h, N_0)}{[D(h)]^2}.$$

The variation of $\frac{\partial}{\partial h} Z_{OM}(h, N_0)$ is shown in Fig. 11(a) for different values of N_0 . It may be noted that $\frac{\partial}{\partial h} Z_{OM}(h, N_0)$ is negative, which proves decreasing nature of $Z_{OM}(h, N_0)$ against h .

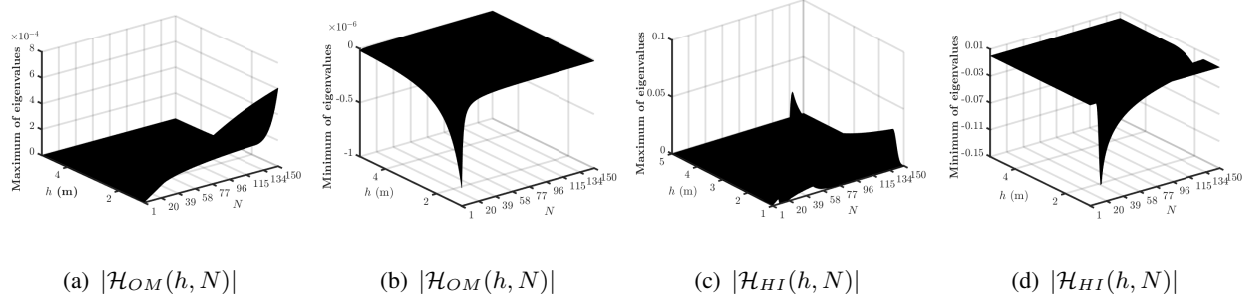


Figure 10: Variation of maximum and minimum eigenvalue against hovering altitude h and antenna array N .

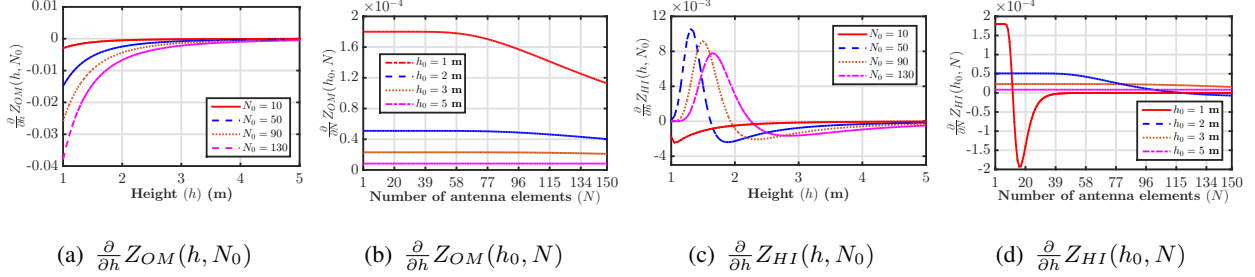


Figure 11: Variation of different derivatives.

F. Proof of Lemma 4

The derivative of $Z_{OM}(h, N)$ with respect to N for a given value of $h = h_0$ is obtained as: $\frac{\partial}{\partial N} Z_{OM}(h_0, N) = \frac{P_{cov}^{(OM)}(h_0, N) + N_N P_{cov}^{(OM)}(h_0, N)}{D(h_0)}$. The variation of $\frac{\partial}{\partial N} Z_{OM}(h_0, N)$ is shown in Fig. 11(b) for different values of h_0 . It may be observed that $\frac{\partial}{\partial N} Z_{OM}(h_0, N)$ is positive, which proves the increasing nature of $Z_{OM}(h_0, N)$ against N .

G. Proof of Theorem 4

For convenience, we denote

$$X(h, N) = -\frac{\frac{\theta_B(N)}{2} - \mu_{HI}(h)}{\sigma_{HI}(h)}, \quad Y(h, N) = \frac{\frac{\theta_B(N)}{2} + \mu_{HI}(h)}{\sigma_{HI}(h)}. \quad (\text{H-1})$$

The derivatives of $X(h, N)$ and $Y(h, N)$ can be obtained by following the same procedure in (E-2) and (E-3), respectively. Then, the derivatives of $P_{cov}^{(HI)}(h, N)$ can be obtained from (E-5). These expressions will be used during the estimation of the Hessian matrix of $Z_{HI}(h, N)$, but they are not given here for brevity.

Now, the Hessian matrix of $Z_{HI}(h, N)$ is given as

$$\mathcal{H}_{HI}(h, N) = \begin{bmatrix} \frac{\partial^2 Z_{HI}(h, N)}{\partial h^2} & \frac{\partial^2 Z_{HI}(h, N)}{\partial h \partial N} \\ \frac{\partial^2 Z_{HI}(h, N)}{\partial N \partial h} & \frac{\partial^2 Z_{HI}(h, N)}{\partial N^2} \end{bmatrix} = \Lambda_0 \begin{bmatrix} h_{11} & h_{12} \\ h_{21} & h_{22} \end{bmatrix}. \quad (\text{H-2})$$

The elements of the Hessian matrix $\mathcal{H}_{HI}(h, N)$ are obtained as

$$h_{11} = N \frac{[D(h)]^2 [D(h)_{hh} P_{cov}^{(HI)}(h, N) - P_{cov}^{(HI)}(h, N) D''(h) - 2D'(h)_h P_{cov}^{(HI)}(h, N)] + 2[D'(h)]^2 P_{cov}^{(HI)}(h, N) D(h)}{[D(h)]^4}.$$

$$h_{12} = h_{21} = \frac{D(h)[{}_h P_{cov}^{(HI)}(h, N) + N_{Nh} P_{cov}^{(HI)}(h, N)] - D'(h)[P_{cov}^{(HI)}(h, N) + N_N P_{cov}^{(HI)}(h, N)]}{[D(h)]^2}.$$

$$h_{22} = \frac{2_N P_{cov}^{(HI)}(h, N) + N_{NN} P_{cov}^{(HI)}(h, N)}{D(h)}, \quad (Z_{HI}(h, N) \text{ is continuous, hence } h_{12} = h_{21}).$$

For a function to be convex, the Hessian matrix should be positive semidefinite. The variation of the eigenvalues of $|\mathcal{H}_{HI}(h, N)|$ against h and N is shown in Fig. 10 (c) and (d). The presence of eigenvalues of opposite sign ensures that $\mathcal{H}_{HI}(h, N)$ is not a convex function of h and N .

H. Proof of Lemma 5

For a function to be unimodal, the sign of the derivative changes only once. The derivative of $Z_{HI}(h, N)$ given in (26) with respect to h for a given $N = N_0$ is found as: $\frac{\partial}{\partial h} Z_{HI}(h, N_0) = N_0 \frac{D(h) {}_h P_{cov}(h, N_0) - D'(h) P_{cov}(h, N_0)}{[D(h)]^2}$. The variation of $\frac{\partial}{\partial h} Z_{HI}(h, N_0)$ is shown in Fig. 11(c) for different values of N_0 . It may be noted that $\frac{\partial}{\partial h} Z_{HI}(h, N_0)$ changes its sign at most once, which proves the unimodal nature of $Z_{HI}(h, N_0)$ against h .

I. Proof of Lemma 6

For a function to be unimodal, the sign of the derivative changes only once. The derivative of $Z_{HI}(h, N)$ given in (26) with respect to N for a given $h = h_0$ is found as: $\frac{\partial}{\partial N} Z_{HI}(h_0, N) = \frac{P_{cov}(h_0, N) + N_N P_{cov}(h_0, N)}{D(h_0)}$. The variation of $\frac{\partial}{\partial N} Z_{HI}(h_0, N)$ is shown in Fig. 11(d) for different values of h . It may be noted that $\frac{\partial}{\partial N} Z_{HI}(h_0, N)$ changes its sign at most once, which proves the unimodal nature of $Z_{HI}(h_0, N)$ against N .

REFERENCES

- [1] M. Mozaffari *et al.*, "A tutorial on UAVs for wireless networks: Applications, challenges, and open problems," *IEEE Commun. Surveys Tuts.*, vol. 21, no. 3, pp. 2334–2360, 3rd Quart. 2019.
- [2] J. Xu, Y. Zeng, and R. Zhang, "UAV-enabled wireless power transfer: Trajectory design and energy region characterization," in *Proc. IEEE Globecom Wksp.*, Singapore, Dec. 2017, pp. 1–7.
- [3] S. Han *et al.*, "Big data enabled mobile network design for 5G and beyond," *IEEE Commun. Mag.*, vol. 55, no. 9, pp. 150–157, Sept. 2017.
- [4] B. Martinez *et al.*, "The power of models: Modeling power consumption for IoT devices," vol. 15, no. 10, pp. 5777–5789, Oct. 2015.
- [5] A. Al-Fuqaha *et al.*, "Internet of Things: A survey on enabling technologies, protocols, and applications," *IEEE Commun. Surveys Tuts.*, vol. 17, no. 4, pp. 2347–2376, 4th Quart. 2015.
- [6] B. A. Coll-Perales, J. Gozalvez, and J. L. Maestre, "5G and beyond: Smart devices as part of the network fabric," *IEEE Netw.*, vol. 33, no. 4, pp. 170–177, July/Aug. 2019.

- [7] W. Saad, M. Bennis, and M. Chen, "A vision of 6G wireless systems: Applications, trends, technologies, and open research problems," *IEEE Network*, vol. 34, no. 3, pp. 134–142, 2020.
- [8] M. Giordani *et al.*, "Toward 6G networks: Use cases and technologies," *IEEE Communications Magazine*, vol. 58, no. 3, pp. 55–61, 2020.
- [9] B. Clerckx *et al.*, "Fundamentals of wireless information and power transfer: From RF energy harvester models to signal and system designs," *IEEE J. Sel. Areas Commun.*, vol. 37, no. 1, pp. 4–33, Jan. 2019.
- [10] Powercast. [Online]. Available: <http://www.powercastco.com>
- [11] J. Xu, Y. Zeng, and R. Zhang, "UAV-enabled wireless power transfer: Trajectory design and energy optimization," *IEEE Trans. Wireless Commun.*, vol. 17, no. 8, pp. 5092–5106, Aug. 2018.
- [12] Y. Hu *et al.*, "Optimal 1D trajectory design for UAV-enabled multiuser wireless power transfer," *IEEE Trans. Commun.*, vol. 67, no. 8, pp. 5674–5688, Aug. 2019.
- [13] J. Chen *et al.*, "Q-charge: A quadcopter-based wireless charging platform for large-scale sensing applications," *IEEE Netw.*, vol. 31, no. 6, pp. 56–61, Nov. 2017.
- [14] H. Wang *et al.*, "Resource allocation for energy harvesting-powered D2D communication underlaying UAV-assisted networks," *IEEE Trans. Green Commun. Netw.*, vol. 2, no. 1, pp. 14–24, Mar. 2018.
- [15] Z. Yang, W. Xu, and M. Shikh-Bahaei, "Energy efficient UAV communication with energy harvesting," *IEEE Trans. Veh. Technol.*, vol. 69, no. 2, pp. 1913–1927, Feb. 2020.
- [16] S. Yin *et al.*, "UAV-assisted cooperative communications with time-sharing information and power transfer," *IEEE Trans. Veh. Technol.*, vol. 69, no. 2, pp. 1554–1567, Feb. 2020.
- [17] D. N. K. Jayakody *et al.*, "Self-energized UAV-assisted scheme for cooperative wireless relay networks," *IEEE Trans. Veh. Technol.*, vol. 69, no. 1, pp. 578–592, Jan. 2020.
- [18] X. Wang and M. C. Gursoy, "Coverage analysis for energy-harvesting UAV-assisted mmWave cellular networks," *IEEE J. Sel. Areas Commun.*, vol. 37, no. 12, pp. 2832–2850, Dec. 2019.
- [19] J. Cui *et al.*, "Unsupervised learning approaches for user clustering in NOMA enabled aerial SWIPT networks," in *Proc. IEEE Int. Wksp. Signal Process. Advances Wireless Commun. (SPAWC)*, Cannes, France, July 2019, pp. 1–5.
- [20] F. Zhou *et al.*, "Computation rate maximization in UAV-enabled wireless-powered mobile-edge computing systems," *IEEE J. Sel. Areas Commun.*, vol. 36, no. 9, pp. 1927–1941, Sept. 2018.
- [21] Y. Du *et al.*, "Joint resources and workflow scheduling in UAV-enabled wirelessly-powered MEC for IoT systems," *IEEE Trans. Veh. Technol.*, vol. 68, no. 10, pp. 10 187–10 200, Oct. 2019.
- [22] S. Suman and S. De, "Optimal UAV-aided RFET system design in presence of hovering inaccuracy," *IEEE Trans. Commun.*, vol. 69, no. 1, p. 558–572, Jan. 2021.
- [23] S. Kumar, S. Suman, and S. De, "Dynamic resource allocation in UAV-enabled mmWave communication networks," *IEEE Internet of Things J.*, vol. 8, no. 12, pp. 9920–9933, June 2021.
- [24] Y. Ma, J. Li, and R. Xu, "Design of an omnidirectional circularly polarized antenna," *IEEE Antennas Wireless Propag. Lett.*, vol. 16, pp. 226–229, 2017.
- [25] E. Boshkovska *et al.*, "Practical non-linear energy harvesting model and resource allocation for SWIPT systems," *IEEE Commun. Lett.*, vol. 19, no. 12, pp. 2082–2085, Dec. 2015.
- [26] C. T. Russell, "Geophysical coordinate transformations," *Cosmic Electrodynamics*, vol. 2, no. 2, pp. 184–196, 1971.